

# Journal of Materials Chemistry A

Accepted Manuscript



This is an *Accepted Manuscript*, which has been through the Royal Society of Chemistry peer review process and has been accepted for publication.

*Accepted Manuscripts* are published online shortly after acceptance, before technical editing, formatting and proof reading. Using this free service, authors can make their results available to the community, in citable form, before we publish the edited article. We will replace this *Accepted Manuscript* with the edited and formatted *Advance Article* as soon as it is available.

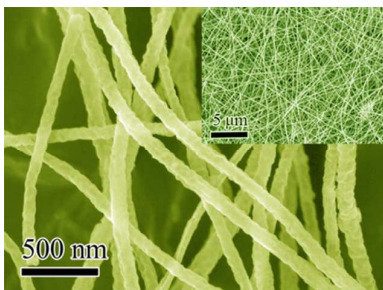
You can find more information about *Accepted Manuscripts* in the [Information for Authors](#).

Please note that technical editing may introduce minor changes to the text and/or graphics, which may alter content. The journal's standard [Terms & Conditions](#) and the [Ethical guidelines](#) still apply. In no event shall the Royal Society of Chemistry be held responsible for any errors or omissions in this *Accepted Manuscript* or any consequences arising from the use of any information it contains.

**For table of contents entry**

Porous Cr-doped SrTiO<sub>3</sub> nanotubes by electrospinning exhibit enhanced photocatalytic activity for removal of azo dye and NO under visible-light irradiation.

Graphic Abstract:



Cite this: DOI: 10.1039/c0xx00000x

www.rsc.org/xxxxxx

ARTICLE TYPE

# Facile fabrication of porous Cr-doped SrTiO<sub>3</sub> nanotubes by electrospinning and their enhanced visible-light-driven photocatalytic properties

Dongfang Hou,<sup>a,b</sup> Xianluo Hu,<sup>b,\*</sup> Wingkei Ho,<sup>c,\*</sup> Pei Hu<sup>b</sup> and Yunhui Huang<sup>b</sup>

Received (in XXX, XXX) Xth XXXXXXXXXX 20XX, Accepted Xth XXXXXXXXXX 20XX

DOI: 10.1039/b000000x

Novel porous Cr-doped SrTiO<sub>3</sub> nanotubes were fabricated using a simple and economical electrospinning technique with subsequent calcination. The average outer diameter of the nanotube was approximately 100 nm, and the multimodal porous netlike framework with high specific surface area was favorable for light harvesting and matter diffusion. Photocatalytic activity was evaluated by degradation of azo dye acid orange 7 and removal of NO under visible light irradiation. The enhanced photocatalytic activity of porous Cr-doped SrTiO<sub>3</sub> nanotubes was attributed to the one-dimensional tube-like architecture, high specific surface area, multimodal pore size distribution, and proper Cr doping.

## Introduction

The growing environmental concerns related to the growth of industrialization and fossil fuel use are becoming an overwhelming problem worldwide.<sup>1,2</sup> Organic pollutants in water and gaseous pollutants (e.g., NO<sub>x</sub>, SO<sub>2</sub>, and carbonyl compounds) are significantly dangerous and can cause numerous human health risks.<sup>3-5</sup> Semiconductor-mediated photocatalytic purification of wastewater and polluted air is a promising environmental remediation technology. Considerable efforts have been made to produce novel and highly efficient semiconductor photocatalysts that can work directly under visible light via crystal growth, doping, and heterostructuring design.<sup>6-9</sup> Various synthetic strategies have been developed to control the morphology of photocatalysts at a nanoscale, which result in large surface areas, abundant surface states, and enhanced photocatalytic performances.<sup>10</sup>

One-dimensional (1D) semiconductor photocatalysts (e.g., nanowires, nanotubes, and nanofibers) have recently attracted researchers because of their high surface areas and porosities.<sup>11</sup> The keen interest in the use of nanotubes is due to their large surface area, which allows several surface atoms to participate in surface reactions.<sup>12</sup> The efficient migration of electrons and holes to the nanotube surface allows them to participate in chemical reactions before recombination, which is vital to enhancing the efficiency of photocatalysts.<sup>12</sup> Researchers are considering the potential of porous materials with hierarchically multimodal pore size distributions as excellent photocatalysts because these materials provide a readily accessible light and matter transfer pathway that can result in enhanced light utilization efficiency and active site.<sup>13, 14</sup> The control of multimodal porosity is complicated and is achieved by combining suitable templates for the required length scale organization.<sup>15</sup> Facile, template-free synthesis of high surface area materials with multiple porous structures remains challenging. Electrospinning is the most

convenient and direct technique for the fabrication of continuous porous 1D nanofibers and nanotubes with small diameters (down to a few nanometers) and is prevalent because of its low cost, versatility, and ease of manufacturing.<sup>16-18</sup> Semiconductor photocatalysts with 1D porous nanostructures exhibit enhanced photocatalytic activities.<sup>15, 19, 20</sup>

Strontium titanate (SrTiO<sub>3</sub>, STO), a well-known cubic-perovskite-oxide with ABO<sub>3</sub> structure, has been studied as a functional material because of its wide application in photocatalysts, photoelectrodes for dye-sensitized solar cells, storage batteries, and oxygen gas sensors.<sup>21</sup> Especially, SrTiO<sub>3</sub> is a promising photocatalyst for water splitting,<sup>22</sup> decomposition of dye,<sup>21</sup> CO<sub>2</sub> reduction,<sup>23</sup> and oxidative destruction of NO<sup>24</sup>. However, SrTiO<sub>3</sub> can only utilize the ultraviolet part of the solar spectrum because of its relatively large band gap (approximately 3.2 eV). One of the effective approaches to improving its photocatalytic efficiency is to modify the band structure of SrTiO<sub>3</sub> by doping foreign elements to shift its optical absorption edge to the visible light region.<sup>25-29</sup> Most SrTiO<sub>3</sub> crystallites prepared via sol-gel methods or traditional solid-state reactions suffer from coarse crystal grain sizes and low surface areas, which significantly restrict further enhancement of photocatalytic activity.<sup>30, 31</sup> So far, only a few studies have modified the microstructure control of SrTiO<sub>3</sub> photocatalysts to minimize intra-diffusion resistance and enhance photoabsorption efficiency. Some 1D SrTiO<sub>3</sub> nanotube photocatalysts have recently been synthesized via different approaches. Liu *et al.*<sup>32</sup> reported that ordered Ag-SrTiO<sub>3</sub> nanotube arrays synthesized via a combination of anodic oxidation, hydrothermal process, and photocatalytic reduction method exhibited excellent photocatalytic activity for hydrogen production under UV light irradiation. TiO<sub>2</sub> nanotube arrays formed on a Ti substrate via electrochemical anodization have been converted into TiO<sub>2</sub>/SrTiO<sub>3</sub> heterostructure nanotubes via controlled substitution of Sr under hydrothermal conditions and exhibited enhanced

photoelectrochemical performance.<sup>33</sup> A heterostructured SrTiO<sub>3</sub>/TiO<sub>2</sub> nanotube array film was fabricated by converting a highly ordered TiO<sub>2</sub> nanotube film via hydrothermal method, which presented high separation efficiency for the photogenerated electron hole pairs. However, these methods are complicated and require multiple steps.<sup>34</sup>

Thus, we develop a facile and economical electrospinning technique for fabricating 1D porous Cr-doped SrTiO<sub>3</sub> nanotubes with average outer diameters of approximately 100 nm without using templates or additives. Porous Cr-doped SrTiO<sub>3</sub> nanotubes are composed of a multimodal porous netlike framework with high specific surface area. Photocatalytic activity was evaluated through the degradation of azo dye acid orange (AO7) and removal of NO at the ppb level under visible light irradiation. Photocatalytic performance of SrTiO<sub>3</sub> nanotubes can be modified by changing the Cr-doped content.

## Experimental

### Material synthesis

Tetrabutyl titanate (TBT), Cr(NO<sub>3</sub>)<sub>3</sub>·9H<sub>2</sub>O, and N,N-dimethylformamide (DMF) were of analytical grade and supplied by Shanghai Sinopharm Chemical Reagent Co. Ltd., China. Polyacrylonitrile (PAN) and Sr(acac)<sub>2</sub> were obtained from Aladdin Chemical Co., Ltd. All chemicals were used as received without further purification.

The precursor solution for electrospinning was prepared by dissolving 0.57 g of Sr(acac)<sub>2</sub> and 0.68 g of TBT in 20 mL of DMF at room temperature according to stoichiometric composition. After stirring for 1 h, 1.6 g of PAN and Cr(NO<sub>3</sub>)<sub>3</sub>·9H<sub>2</sub>O were added into the mixture. The mixture was stirred overnight and resulted in a transparent precursor solution. The precursor solution was inserted into a plastic syringe with a 20-gauge stainless steel needle. The feeding rate was 0.7 mL h<sup>-1</sup>, monitored by a syringe pump. The electrode-clamped metallic needle was connected to a variable high-voltage power supply. A collection of aluminum foil acted as a grounded counter electrode, 12 cm away from the needle tip. Sr(acac)<sub>2</sub>/TBT/Cr(NO<sub>3</sub>)<sub>3</sub>/PAN composite nanofibers formed when 15 kV was applied. The as-collected electrospun precursor fibers were air-dried at 80 °C for 6 h. Subsequently, the composite fibers were calcined in air for 1 h at 600 °C with a heating rate of 1 °C min<sup>-1</sup>. The as-prepared samples were labelled STO, Cr1-STO, Cr2-STO, Cr4-STO, and Cr6-STO according to the corresponding atom ratios of Cr to Sr (0%, 1%, 2%, 4%, and 6%, respectively).

### Materials characterization

X-ray diffraction (XRD) analysis was performed using a Rigaku D/MAX-RB diffractometer with filtered Cu Kα radiation. Full diffraction patterns were taken in the 2θ range from 10° to 80° at a step model with a 0.02° step size. The sample morphology was characterized using field emission scanning electron microscopy (FE-SEM; SIRION200, Holland; accelerating voltage: 10 kV). Transmission electron microscopy (TEM) and high-resolution transmission electron microscopy images were recorded using a JEOL JEM-2010F microscope. X-ray photoelectron spectroscopy (XPS) measurements were performed on a VG MultiLab 2000

system with a monochromatic Al Kα X-ray source (ThermoVG Scientific). The Brunauer–Emmett–Teller (BET) surface area was determined via N<sub>2</sub> adsorption using a Micromeritics ASAP 2020 analyzer. The photoluminescence emission spectra of the samples were recorded using a Hitachi F-4500 fluorescence spectrophotometer at room temperature to investigate the recombination of photoinduced charge carriers. UV-vis diffuse reflectance spectra (DRS) were recorded on a SHIMADZU UV-2550 spectrophotometer with an integrating sphere using BaSO<sub>4</sub> as the reference.

### Activity Evaluation

Photocatalytic activity was evaluated through the degradation of AO7 and removal of NO at the ppb level in a continuous flow reactor under visible light irradiation at ambient temperature. A photochemical reactor of self-made cylindrical glass vessel with a water-cooling jacket was used in the photocatalytic degradation of AO7. A 500 W Xe lamp with a 400 nm cut-off filter was chosen as the visible light source. The irradiation distance between the lamp and the sample was 12 cm. The 80 mg photocatalyst was uniformly dispersed into the reactor with 80 mL of AO7 solution (10 g L<sup>-1</sup>). Before irradiation, the suspension was stirred for 30 min and kept in the dark until an adsorption–desorption equilibrium was reached. At a certain time interval, 3 mL of the reaction solution was taken, centrifuged, and measured on a UV-vis spectrometer at a maximum absorption wavelength of 485 nm. In the removal of NO, the volume of the rectangular reactor, which was made of stainless steel and covered with Saint-Glass, was 4.5 L (30 cm × 15 cm × 10 cm). A 30 W commercial LED lamp (λ = 448 nm) was placed vertically on the reactor. A 0.1 g photocatalyst was coated into a dish with a 12 cm diameter. The NO gas was obtained from a compressed gas cylinder at a concentration of 50 ppm of NO (N<sub>2</sub> balance) and diluted to approximately 600 ppb using a dynamic gas calibrator (Ecotech GasCal 1000) with zero air supply. The gas streams were pre-mixed completely using a gas blender. The flow rate was controlled at 1000 mL min<sup>-1</sup> by a mass flow controller. After achieving an adsorption–desorption equilibrium, the lamp was turned on. The concentration of NO was continuously measured using the NO<sub>x</sub> analyzer model T200 (Teledyne API). The removal ratio (δ) of NO was calculated as  $\delta(\%) = (1 - C/C_0) \times 100\%$ , where C<sub>0</sub> is the initial NO concentration, and C is the NO concentration after the photocatalytic reaction.

## Results and discussion

Fig. 1 shows the XRD results of the products obtained from annealing as-spun precursor nanofibers in air for 1 h at 600 °C. All products were well crystallized, and the diffraction peaks of STO, Cr1-STO, Cr2-STO, Cr4-STO, and Cr6-STO were readily indexed to cubic SrTiO<sub>3</sub> (JCPDS 35-0734). No signals from other impurities were observed. Fig. 1b shows a detailed analysis of the (110) diffraction peaks in the range of 2θ = 32° to 33°. The position peaks of Cr1-STO, Cr2-STO, Cr4-STO, and Cr6-STO slightly shifted to a larger 2θ value as Cr content increased. It maybe indicates that Cr ions were incorporated into the SrTiO<sub>3</sub> lattice and slightly caused lattice deformations.

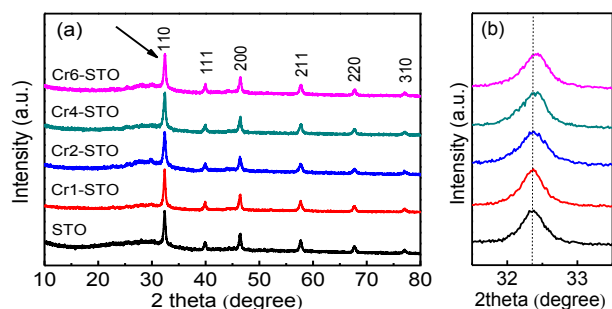


**Fig. 1** (a) XRD patterns of STO, Cr1-STO, Cr2-STO, Cr4-STO, and Cr6-STO obtained from annealing the as-spun precursor nanofibers at 600 °C, and (b) (110) diffraction peak positions in the range of  $2\theta = 32^\circ$  to  $33^\circ$ .

Product morphology was observed via FE-SEM. Long  $\text{Sr}(\text{acac})_2/\text{TBT}/\text{Cr}(\text{NO}_3)_3/\text{PAN}$  precursor nanofibers with diameters of approximately 200 nm were obtained by electrospinning (Fig. 2a). The product surface was smooth. After annealing the precursor nanofibers at 600 °C, the  $\text{SrTiO}_3$  nanofibers with diameters of approximately 100 nm formed. These nanofibers were smaller than the precursor nanofibers because of the decomposition of PAN, TBT,  $\text{Cr}(\text{NO}_3)_3$ , and  $\text{Bi}(\text{NO}_3)_3$  (Figs. 2b to 2d). These nanofibers with tough irregular surfaces were as long as several millimeters and piled up disorderly (Fig. 2b). Fig. 2c shows a representative FE-SEM image of the  $\text{SrTiO}_3$  nanotubes, which reveals that all nanofibers transformed into nanotubes after annealing. These continuous nanotubes were porous and composed of interlinked nanoparticles. Fig. 2d shows several clear nozzles of Cr4-STO nanotubes. All products exhibited tubular structures, which indicate no significant difference on tubular morphology after the introduction of Cr ions.

The TEM images provided further insight into the

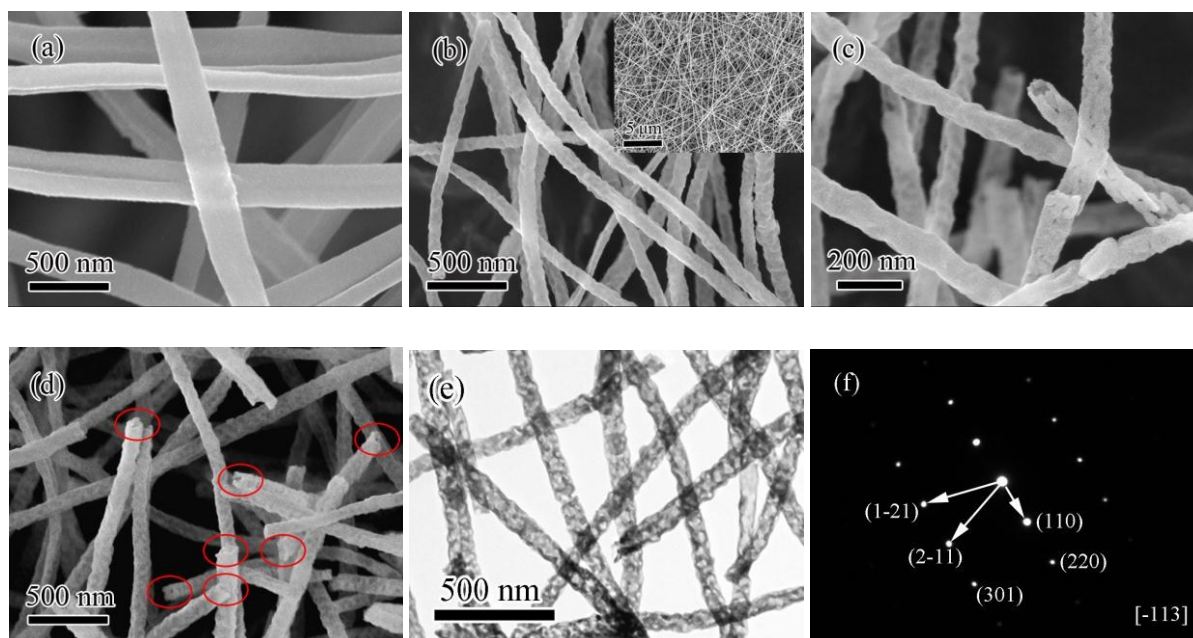


**Fig. 2** Representative FE-SEM images: (a) as-spun precursor nanofibers of STO, (b) STO nanotubes obtained at 600 °C, (c) porous tubular structures of STO, (d) Cr4-STO nanotubes obtained at 600 °C, (e) TEM image of STO nanotubes obtained at 600 °C, and (f) SAED pattern of STO nanotubes.

microstructure of porous STO nanotubes. Fig. 2e shows a representative TEM image for the STO product, which reveals a well-defined tubular and porous morphology. The individual STO nanotube had a continuous structure and uniform diameter. The nanotube walls comprised of interconnected nanocrystals and numerous pores with different sizes, similar to the SEM observation. Fig. 2f displays a selected area electron diffraction pattern, showing that the as-formed STO nanoparticles were single-crystalline by nature. The nanoparticles could be indexed to the  $[-113]$  zone axis of cubic-structured  $\text{SrTiO}_3$ , which is consistent with the XRD results. A tubular architecture is very beneficial in the catalyst design and provided an effective electron percolation pathway that can significantly improve the lifetime of photogenerated charge carriers.<sup>35</sup> Thus, porous nanotubes with high surface areas could further enhance the absorption of photon energy and benefit photocatalytic efficiency.

Various factors (e.g., raw materials, condensation reaction during sol gelation, electrospinning parameters, and sintering process) influence the morphology of electrospun fibers.<sup>16</sup> Figs. S1a to S1d display the TEM images of the products obtained from annealing the as-spun precursor nanofibers at 300, 400, 500, and 600 °C, respectively. After annealing at 300 °C, the diameter slightly decreased, and the surface was no longer smooth (Fig. S1a). Numerous pores in the nanofibers emerged and gradually enlarged when annealing at 400, 500, and 600 °C and increasing calcination temperature. The hollow structure, annealing at 400 °C, loomed up even if the boundaries were blurred. When the temperature increased to 500 °C, tough irregular surfaces were observed outside and inside the nanotubes. The nanotubes with thicker walls were also exhibited in the inset of Fig. S1b and S1c. Fig. S1d shows distinct porous nanotubes with diameters of 100 nm and wall thicknesses of 10 nm to 20 nm. The enlargement of pores in the wall and hollow structure can increase the surface area. According to the TEM observations of the hollow nanofiber

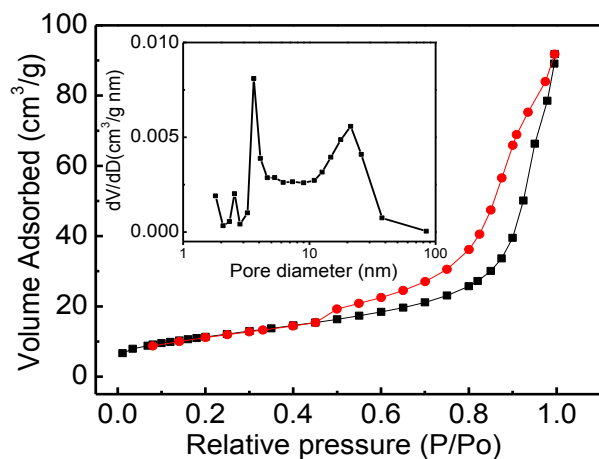


Fig. 3 N<sub>2</sub> adsorption–desorption isotherms of Cr4–STO and pore size distribution of Cr4–STO (inset).

formation, the interaction between the Sr and Ti precursors and the different mass transfer rates during the heating process prompted nanotube formation. PAN was a sacrificial template and was gradually decomposed during the calcination process, contributing to its fibrous structure. The precursors on the surface region of the as-spun nanofibers were quickly decomposed oxidatively to generate SrTiO<sub>3</sub> nanocrystals during calcination. Most precursors in the core region did not react promptly because of the lack of oxygen and were redistributed via fast surface

diffusion, which resulted in a concentration gradient, leading to the Kirkendall effect.<sup>36,37</sup> PAN decomposed completely when the heating temperature was further enhanced, and a hollow structure was established. Fig. 3 shows N<sub>2</sub> adsorption–desorption isotherms, and the pore size distribution curves of Cr4–STO. The isotherm is of type IV (BDDT classification) with a hysteresis loop in the range of (0.4 to 1.0)  $P/P_0$ , which indicates pore size distributions in the mesoporous region. The specific surface area of the samples, calculated by the multipoint BET method, was 40.5 m<sup>2</sup> g<sup>-1</sup>. The pore size distribution of Cr4–STO, calculated from the desorption branch of the N<sub>2</sub> isotherm via the Barrett–Joyner–Halenda method (Fig. 3, inset), shows a relative wide range of mesopores. The porous nanotubes contained small (peak pore diameter, ca. 4 nm) and large mesopores (peak pore diameter, ca. 25 nm) in the holes of the porous nanotube walls. The N<sub>2</sub> adsorption–desorption analyses could not provide further macroporous information for the 3D networks composed of Cr4–STO nanotubes. However, a large number of macropores were observed among the disorderly nanotubes. Some of the macropores had diameters up to several micrometers, which could be confirmed by SEM and TEM analyses.

The results highlight a facile process for synthesizing SrTiO<sub>3</sub> and Cr-doped SrTiO<sub>3</sub> nanotubes with macroporous and mesoporous structures with no templates or additives. The prepared nanotubes had at least three structural organization levels: (i) SrTiO<sub>3</sub> crystallization at a nanoscale, (ii) SrTiO<sub>3</sub> nanotubes with continuous mesoporous walls and bimodal peak mesopores from 2 nm to 50 nm, and (iii) 3D netlike macroporous

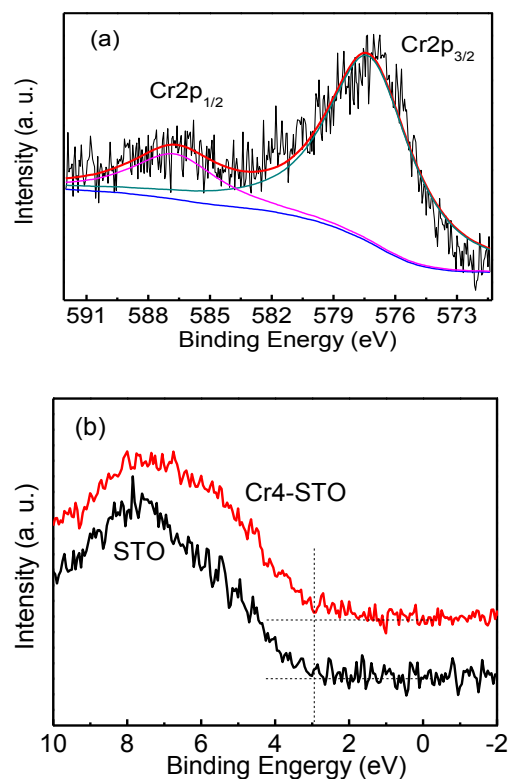


Fig. 4 High-resolution XPS spectra of Cr4–STO: (a) Cr 2p and (b) VB XPS spectra of STO and Cr4–STO.

frameworks formed from stacking nanotubes at a micrometer scale. Mesoporous materials possessed large surface areas and several active sites. Macroporous frameworks could serve as light transfer paths for the distribution of photon energy and solution and as gas transfer paths for the large surfaces of inner photoactive mesoporous nanotubes. All these characteristics benefited the photoreaction.<sup>13,14</sup>

XPS can further provide important information on the surface chemical state and composition of Cr4–STO nanotubes. The nanotubes were composed of Sr, Ti, Cr, and O. The 3d peaks of Sr were also examined via high-resolution XPS (Fig. 2Sa). The XPS peaks at 134.3 and 132.6 eV were assigned to Sr 3d<sub>3/2</sub> and Sr 3d<sub>5/2</sub>, respectively, and ascribed to Sr (+2) in Cr4–STO. The Ti 2p<sub>3/2</sub> and Ti 2p<sub>1/2</sub> peaks with a typical spin-orbit doublet of 5.7 eV were at 458.3 and 464.0 eV, respectively, which are characteristic of Ti (IV) (Fig. 2Sb). Fig. 4a shows the deconvoluted Cr 2p spectrum. Two peaks at 586.7 eV for Cr 2p<sub>1/2</sub> and 577 eV for Cr 2p<sub>3/2</sub> were observed, which indicated the Cr (+3) state in Cr4–STO. Wei *et al.*<sup>26</sup> reported that the photocatalytic activity of SrTiO<sub>3</sub> doped with Cr at a Sr site under visible light was higher than that at a Ti site. The (110) diffraction peaks for the XRD pattern shift toward a higher  $2\theta$  value (Fig. 1b), which implies that Cr<sup>3+</sup> was incorporated into the Sr<sup>2+</sup> (ionic radius: 0.118 nm) sites in the SrTiO<sub>3</sub> lattice. Otherwise, the 110 diffraction peaks would have shifted toward a lower  $2\theta$  value or would have not shifted at all because the ionic radius of Cr<sup>3+</sup> (ionic radius: 0.062 nm) was slightly larger than that of Ti<sup>4+</sup> (ionic radius: 0.061 nm).<sup>27,38</sup> In the XPS analysis, not only information on the binding energy of a specific element was obtained but also the total

density of states of the valence band (VB). Fig. 4b shows the VB XPS spectra of the STO and Cr4-STO nanotubes. The additional diffusive electronic states of Cr4-STO above the VB maximum (VBM) were observed, indicating a mid-gap near the top of the VB. Previous studies demonstrated that several Cr 3d gap states inserted into the band gap of SrTiO<sub>3</sub> in Cr-doped SrTiO<sub>3</sub> and resulted in visible light absorption.<sup>26,27</sup> The formation of mid-gap was ascribed to the Cr 3d gap states in Cr4-STO, which modified the SrTiO<sub>3</sub> band structure.<sup>39</sup>

The optical properties of all products were measured using the UV-vis diffuse reflection spectrum with a wavelength range from 200 nm to 800 nm (Fig. 5). The STO nanotubes showed an absorbance edge at approximately 397 nm. The Cr-doped SrTiO<sub>3</sub> nanotubes possessed better responsibility to visible light than SrTiO<sub>3</sub> nanotubes, and a red shift of absorption edge was observed when Cr content increased. The enhanced light response was attributed to the interaction between the Cr element and the SrTiO<sub>3</sub> lattice. Compared with the SrTiO<sub>3</sub> nanotubes, the Cr4-STO nanotubes exhibited a significant absorption tail in the range of 350 to 550 nm. It indicated that Cr<sup>3+</sup> ions can be incorporated into the SrTiO<sub>3</sub> lattice and produce new Cr 3d gap states that correspond to the XPS results of Cr4-STO nanotubes. The electronic structure of Cr4-STO was narrowed by the new Cr 3d gap states and enhanced photocatalytic activity.<sup>27</sup> The band-gap values were calculated from the UV-vis absorption spectra according to the following equation:

$$ahv = A (hv - E_g)^{n/2}$$

where  $a$ ,  $hv$ ,  $A$ , and  $E_g$  are the absorption coefficient, photo energy, proportionality constant, and gap band, respectively.  $n$  is equal to 1 or 4 depending on a direct or indirect transition. The fundamental SrTiO<sub>3</sub> absorption exhibited an indirect transition between bands;<sup>26</sup> thus,  $n = 4$ . The band gap energy was calculated by extrapolating a straight line to the abscissa axis. Fig. 5b (inset) shows the plot of the  $(ahv)^{1/2}$  versus  $hv$ . The band gaps of STO, Cr1-STO, Cr2-STO, Cr4-STO, and Cr6-STO were estimated as 3.12, 2.32, 2.26, 2.12, and 2.19 eV, respectively. Differences in the band gap were due to the various Cr content in the SrTiO<sub>3</sub> lattice and its influence on the band structure.

The recombination of photo-induced electrons and holes did not favor photocatalyst activities. The photoluminescence (PL) emission spectra were used to evaluate the separation capability of photoinduced carriers. The PL emission spectra explained the efficiency of charge carrier trapping, immigration, and transfer rate of photogenerated electron hole pairs in the semiconductor.<sup>40</sup>

High PL intensities indicated high recombination rates of photogenerated electrons and holes. Fig. 6 shows the room temperature PL emission spectra of STO, Cr1-STO, Cr2-STO, Cr4-STO, and Cr6-STO nanotubes. The shape of these curves is similar and asymmetrical, but the peak positions seem a little shift. This may be assigned to the change in the electronic structure.<sup>42</sup> When excited at 320 nm, two emission peaks at approximately 430 and 470 nm were observed. The decrease of PL intensities was observed when the Cr content increased, but the PL intensity for Cr6-STO nanotubes was enhanced. By contrast, the emission intensity of Cr4-STO nanotubes clearly decreased, which suggests that the recombination of photogenerated charge carriers can be inhibited effectively. Therefore, Cr4-doped SrTiO<sub>3</sub> nanotubes are highly favorable for efficiently separating photoinduced carriers during photocatalytic reactions. In addition, the asymmetry of curves with different intensity reflects the concentration changes of defects in the samples,<sup>43</sup> which is also related to the photocatalytic activity.

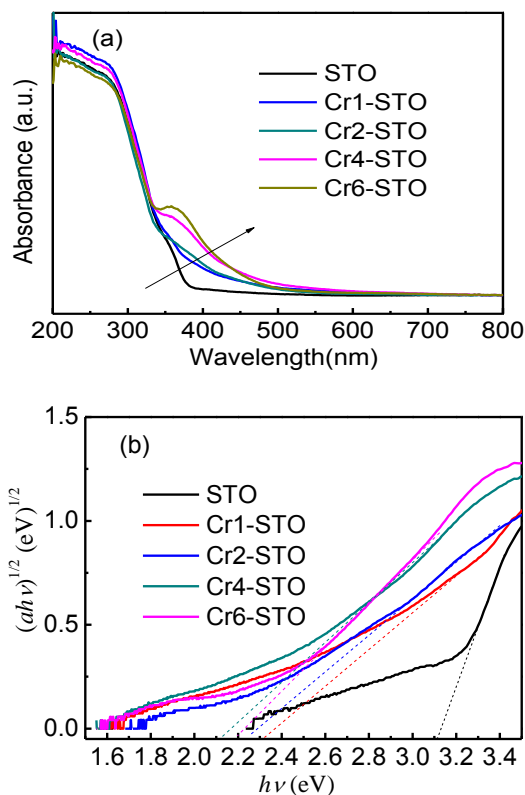


**Fig. 5** (a) UV-vis DRS of STO, Cr1-STO, Cr2-STO, Cr4-STO, and Cr6-STO samples, and (b) relationship between  $(ahv)^{1/2}$  and photon energy.

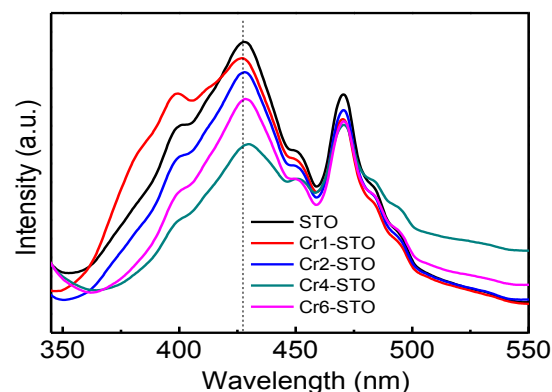


**Fig. 6** Room-temperature PL spectra for STO, Cr1-STO, Cr2-STO, Cr4-STO, and Cr6-STO samples.

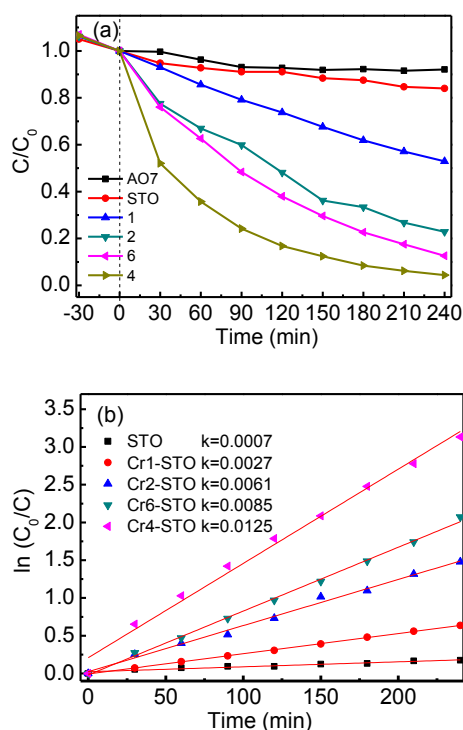


**Fig. 7** (a) Degradation profiles of AO7 over STO, Cr1-STO, Cr2-STO, Cr4-STO, and Cr6-STO, where  $C$  is the RhB concentration and  $C_0$  is the initial AO7 concentration after adsorption-desorption equilibrium. (b) Kinetic linear simulation curves of AO7 photocatalytic degradation with STO, Cr1-STO, Cr2-STO, Cr4-STO, and Cr6-STO.

The photocatalytic activity of nanotubes under visible light illumination ( $\lambda > 400$  nm) was initially determined using AO7 as the model pollutant (Fig. 7a). Prior to light irradiation, the solution was kept in the dark for 30 min to reach adsorption-desorption equilibrium between the photocatalyst and AO7. All samples have the same porous structure and exhibited the similar adsorption performance, leading to the enhanced photocatalytic activity. Fig. 7a shows that AO7 was slightly degraded by the STO nanotubes after visible light irradiation for 240 min. A relatively low photocatalytic activity was observed, whereas self-degradation was negligible. The Cr-doped nanotubes significantly influenced photocatalytic activity. Even with a small amount of Cr, the photocatalytic activity of Cr1-STO nanotubes notably enhanced to 47% after visible light irradiation for 240 min. For the Cr2-STO and Cr4-STO nanotubes, the efficiency of AO7 photodegradation gradually increased to 77% and 95%, respectively. Consequently, the Cr 3d gap states increased, and the SrTiO<sub>3</sub> band gap narrowed, which benefitted photocatalytic activity. The photocatalytic activity of Cr6-STO nanotubes decreased as Cr content increased. For Cr4-STO nanotubes, the efficiency of AO7 photodegradation reached a maximum value.

The degradation of AO7 on STO and Cr-doped SrTiO<sub>3</sub> fits a pseudo-first-order kinetics. The degradation constants ( $k$ ) were calculated as 0.0007, 0.0027, 0.0061, 0.0125, and 0.0085 min<sup>-1</sup> for STO, Cr1-STO, Cr2-STO, Cr4-STO, and Cr6-STO, respectively (Fig. 7b). The Cr4-STO nanotubes exhibited the best

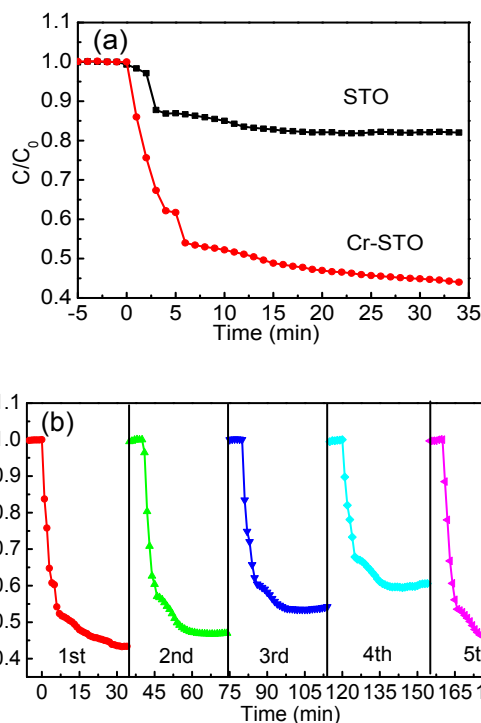


**Fig. 8** (a) Plots of the NO concentration decrease vs. irradiation time in the presence of STO and Cr4-STO nanotubes under visible light irradiation ( $\lambda = 448$  nm). (b) Multiple photocatalytic reaction cycles of Cr4-STO nanotubes for NO removal.

activity on the photo-oxidation of AO7. Cr doping influenced geometric, electronic, and optical properties and introduced lattice distortion and Cr 3d gap states, narrowing the SrTiO<sub>3</sub> band gap.<sup>26</sup> The doped SrTiO<sub>3</sub> with a low Cr dopant concentration exhibited lower photocatalytic activity than that with a high Cr dopant concentration because of the poor mobility of photogenerated electrons.<sup>26</sup> However, excess Cr doping can irritate several lattice distortions and cause recombination centers of photogenerated electrons and holes, decreasing photocatalytic activity.<sup>27, 44</sup>

Both STO and Cr4-STO nanotubes were evaluated through the photocatalytic removal of gaseous NO in air under visible light irradiation ( $\lambda = 448$  nm) to gain further insight into the photocatalytic activity of products and potential ability for air purification. The adsorption-desorption equilibrium between the air with NO and photocatalysts was reached prior to light irradiation. The Cr4-STO nanotubes exhibited higher activity in the removal of gaseous NO than that of STO nanotubes under visible light illumination (Fig. 8a). The Cr4-STO nanotubes removed 56% of NO in 35 min, whereas the STO nanotubes removed only 18%. The photocatalytic activity of Cr4-STO nanotubes was 8.6 times higher than that of STO nanotubes and exhibited a higher NO removal rate at the first 6 min after light irradiation, revealing the superior photocatalytic activity of Cr-doped STO nanotubes. The significantly enhanced photocatalytic activities of porous Cr4-STO nanotubes were attributed to the large surface area, enhanced gas transfer, light harvesting ability, and the narrow band gap due to Cr doping. Photocatalyst stability

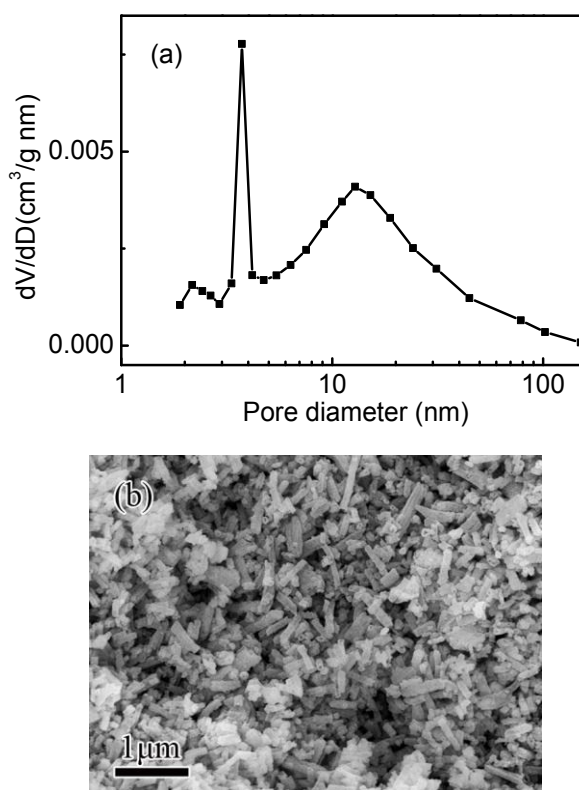


**Fig. 9** (a) Pore size distribution curve of ground Cr4-STO powders, which indicates that the sample still maintains a mesoporous structure. (b) SEM image of ground Cr4-STO powders.

was also important to its practical application. Fig. 8b shows the multiple photocatalytic reaction cycles of Cr4-STO nanotubes for NO removal under visible light irradiation ( $\lambda = 448$  nm). Photocatalytic activity slightly decreased after four cycles, which indicates a slight deactivation of the catalyst. However, photocatalytic efficiency of Cr4-STO nanotubes still maintained up to 42% and was relatively higher than that of STO nanotubes. The most plausible explanation is that some oxidation products (e.g.,  $\text{HNO}_2$  and  $\text{HNO}_3$ ) were generated on the catalyst surface during photocatalysis and blocked a few active sites on the catalyst.<sup>45-47</sup> The photocatalytic activities of Cr4-STO nanotubes in the fifth cycle were almost recovered after being washed with deionized water because  $\text{HNO}_2$  and  $\text{HNO}_3$  were removed, implying that Cr4-STO nanotubes are promising materials for air purification.

The Cr4-STO nanotubes were ground with an agate mortar to destroy the 3D networks of the samples. Their photocatalytic activities were subsequently tested to further substantiate the beneficial influence of 3D netlike frameworks formed from long stacking nanotubes on photocatalytic activity. Fig. S3 shows  $\text{N}_2$  adsorption-desorption isotherms of ground Cr4-STO samples. The isotherm is similar to that of Cr4-STO nanotubes and of type IV (BDDT classification) with a hysteresis loop in the range of (0.4 to 1.0)  $P/P_0$ , which also indicates pore size distributions in the mesoporous region. The specific surface area of the samples, calculated by the multipoint BET method, was  $39.4 \text{ m}^2 \text{ g}^{-1}$ , and the results are close. Fig. 8a shows that the ground samples

maintained their mesoporous structures. However, the macropores from the 3D networks disappeared, and all long nanotubes broke into short hollow rods of less than  $1 \mu\text{m}$  lengths (Fig. 8b). An approximate 9% drop in photocatalytic activity was observed after grinding. Two things account for this decrease: first, the collapse of 3D networks composed of disorderly 1D nanotubes, which caused the macropores that formed among the nanotubes to disappear or decrease and to lessen their ability to transport matter and absorb light, lowering the photocatalytic activity; second, the relativity between the photocatalytic activity and the nanotube length. Liu *et al.*<sup>48</sup> reported that photocatalytic activity increased and then reached saturation as nanotube length increased, which is mainly influenced by the light absorption changes along the nanotube. In addition, the dependence of photocatalytic efficiency on the nanotube length of  $0.5 \mu\text{m}$  to  $10 \mu\text{m}$  indicated that photocatalytic efficiency reached saturation when the nanotube length was approximately  $4 \mu\text{m}$ . The short hollow rods with less than  $1 \mu\text{m}$  lengths after grinding led to decreased light absorption and photocatalytic efficiency.

In general, photocatalytic activity is governed by three properties: photoabsorption efficiency, efficiency of the reaction of photogenerated electrons and holes, and the combination of two. Numerous factors have crucial roles in photocatalysis.<sup>5,42</sup> Some of these factors can explain the high photocatalytic activity of Cr-doped  $\text{SrTiO}_3$  nanotubes.

- (1) 1D nanotube structure. The 1D nanotube structure semiconductor has demonstrated superior performances (e.g., remarkable directional transport characteristics of electrons and holes). These channels could serve as light and matter transfer paths and enhance the photocatalytic activity.
- (2) Multimodal pore size distributions. Multimodal porous architecture with high specific surface areas not only contributes to several active sites but also provides efficient transfer of photogenerated charges, which is highly preferable for harvesting light. The incorporation of macroporous structures into mesoporous materials is important in molecule traffic control and in the resistance of photocatalyst deposit. The porosity of nanotubes not only provides a readily accessible pore wall structure but also optimizes the transport of matter by minimizing the pressure drop.
- (3) Cr doping. Some Cr 3d gap states appear in the band gap of  $\text{SrTiO}_3$  through Cr doping, which narrows the band gap. The optical absorption edge shifts from the UV region to the visible light region and enhances photocatalytic activities.

## Conclusions

Porous Cr-doped  $\text{SrTiO}_3$  nanotubes with average diameters of approximately  $100 \text{ nm}$  were successfully fabricated using a facile and economical electrospinning method combined with subsequent calcinations without using any templates or additives. Porous Cr-doped  $\text{SrTiO}_3$  nanotubes with high specific surface areas showed different pore organizations: fine and large mesopores with peak pore diameters of  $4$  and  $25 \text{ nm}$  and macropores from the holes formed among nanofibers up to the millimeter scale. Cr-doped  $\text{SrTiO}_3$  nanotubes with a 4% Cr/Sr

ratio exhibited high photocatalytic activities for the degradation of AO7 and removal of NO under visible light irradiation because of 1D nanotube structure, high specific surface area, multimodal pore size distributions, and proper Cr doping. These factors decreased the combination of electron holes, enhanced the photocatalysis activities, and improved the photoabsorption efficiency and efficiency of the reaction of photogenerated electrons and holes. Porous Cr-doped SrTiO<sub>3</sub> nanotube frameworks are promising advanced catalytic support and novel optic materials.

## Acknowledgments

This work was supported by the Natural Science Foundation of China (Grant Nos. 21271078, 51472098), NCET (Program for New Century Excellent Talents in University, No. NECT-12-0223), and the Program for Changjiang Scholars and Innovative Research Team in University (PCSIRT). The authors are grateful for the Analytical and Testing Center of HUST for providing the XRD, SEM, and TEM measurements. This research is financially supported by the research grant of Early Career Scheme (ECS 809813) from the Research Grant Council, Hong Kong SAR Government and Dean's Research Fund-Early Career Researchers (04022) from The Hong Kong Institute of Education.

## Notes and references

<sup>a</sup>College of Material and Chemical Engineering, Three Gorges University, Yichang 443002, China

<sup>b</sup>State Key Laboratory of Materials Processing and Die & Mould Technology, School of Materials Science and Engineering, Huazhong University of Science and Technology, Wuhan 430074, China

<sup>c</sup>Department of Science and Environmental Studies, The Centre for Education in Environmental Sustainability, The Hong Kong Institute of Education, Hong Kong, China  
E-mail: huxl@mail.hust.edu.cn (X. L. Hu); keithho@ied.edu.hk (W. K. Ho)

- 1 C. Chen, W. Ma and J. Zhao, *Chem. Soc. Rev.*, 2010, **39**, 4206-4219.
- 2 X. Wang, K. Maeda, A. Thomas, K. Takanabe, G. Xin, J. M. Carlsson, K. Domen and M. Antonietti, *Nat Mater.*, 2009, **8**, 76-80.
- 3 K. Ariga, S. Ishihara, H. Abe, M. Li and J. P. Hill, *J. Mater. Chem.*, 2012, **22**, 2369.
- 4 M. Shang, W. Wang, L. Zhang, S. Sun, L. Wang and L. Zhou, *J. Phys. Chem. C*, 2009, **113**, 14727-14731.
- 5 P. Zhou, J. Yu and M. Jaroniec, *Adv. Mater.*, 2014, **26**, 4920-4935.
- 6 X. L. Hu, G. S. Li and J. C. Yu, *Langmuir*, 2009, **26**, 3031-3039.
- 7 F. Wang, W. K. H. Ng, J. C. Yu, H. Zhu, C. Li, L. Zhang, Z. Liu and Q. Li, *Appl. Catal. B*, 2012, **111-112**, 409-414.
- 8 X. An, J. C. Yu, Y. Wang, Y. Hu, X. Yu and G. Zhang, *J. Mater. Chem.*, 2012, **22**, 8525.
- 9 G. Liu, L. Wang, H. G. Yang, H. Cheng and G. Q. Lu, *J. Mater. Chem.*, 2010, **20**, 831-843.
- 10 H. Tong, S. Ouyang, Y. Bi, N. Umezawa, M. Oshikiri and J. Ye, *Adv. Mater.*, 2012, **24**, 229-251.

- 11 M. Shang, W. Z. Wang, W. Z. Yin, J. Ren, S. M. Sun and L. Zhang, *Chem.-Eur. J.*, 2010, **16**, 11412-11419.
- 12 S. V. N. T. Kuchibhatla, A. S. Karakoti, D. Bera and S. Seal, *Process. Mater. Sci.*, 2007, **52**, 699-913.
- 13 J. Yu, L. Zhang, B. Cheng and Y. Su, *J. Phys. Chem. C*, 2007, **111**, 10582-10589.
- 14 X. Wang, J. C. Yu, C. Ho, Y. Hou and X. Fu, *Langmuir*, 2005, **21**, 2552-2559.
- 15 Y. Long, M. Yu, B. Sun, C. Gu and Z. Fan, *Chem. Soc. Rev.*, 2012, **41**, 4560-4580.
- 16 A. Greiner and J. H. Wendorff, *Angew. Chem. Int. Ed.*, 2007, **46**, 5670-5703.
- 17 N. Bhardwaj and S. C. Kundu, *Biotechnol. Adv.*, 2010, **28**, 325-347.
- 18 Z. Dong, S. J. Kennedy and Y. Wu, *J. Power Sources*, 2011, **196**, 4886-4904.
- 19 D. F. Hou, W. Luo, Y. H. Huang, J. C. Yu and X. L. Hu, *Nanoscale*, 2013, **5**, 2028-2035.
- 20 D. F. Hou, X. L. Hu, P. Hu, W. Zhang, M. F. Zhang and Y. H. Huang, *Nanoscale*, 2013, **5**, 9764-9772.
- 21 T. Cao, Y. Li, C. Wang, C. Shao and Y. Liu, *Langmuir*, 2011, **27**, 2946-2952.
- 22 K. Iwashina and A. Kudo, *J. Am. Chem. Soc.*, 2011, **133**, 13272-13275.
- 23 D. Sui, X. Yin, H. Dong, S. Qin, J. Chen and W. Jiang, *Catal. Lett.*, 2012, **142**, 1202-1210.
- 24 U. Sulaeman, S. Yin and T. Sato, *J. Appl. Phys. Lett.*, 2010, **97**, 103102.
- 25 W. Wei, Y. Dai, M. Guo, L. Yu and B. Huang, *J. Phys. Chem. C*, 2009, **113**, 15046-15050.
- 26 W. Wei, Y. Dai, H. Jin and B. Huang, *J. Phys. D, Appl. Phys.*, 2009, **42**, 055401.
- 27 H. Yu, S. Yan, Z. Li, T. Yu and Z. Zou, *Int. J. Hydrogen Energy*, 2012, **37**, 12120-12127.
- 28 U. Sulaeman, S. Yin and T. Sato, *Appl. Catal. B*, 2011, **105**, 206-210.
- 29 S. Ouyang, H. Tong, N. Umezawa, J. Cao, P. Li, Y. Bi, Y. Zhang and J. Ye, *J. Am. Chem. Soc.*, 2012, **134**, 1974-1977.
- 30 A. Jia, Z. Su, L. Lou and S. Liu, *Solid State Sci.*, 2010, **12**, 1140-1145.
- 31 S. Hara and H. Irie, *Appl. Catal. B*, 2012, **115-116**, 330-335.
- 32 J. Liu, Y. Sun, Z. Li, S. Li and J. Zhao, *Int. J. Hydrogen Energy*, 2011, **36**, 5811-5816.
- 33 J. Zhang, J. H. Bang, C. Tang and P. V. Kamat, *ACS nano*, 2009, **4**, 387-395.
- 34 Y. Zhu, L. Xu, J. Hu, J. Zhang, R. Du and C. Lin, *Electrochim. Acta*, 2014, **121**, 361-368.
- 35 G. Dai, J. Yu and G. Liu, *J. Phys. Chem. C*, 2011, **115**, 7339-7346.
- 36 G. Dong, X. Xiao, M. Peng, Z. Ma, S. Ye, D. Chen, H. Qin, G. Deng, Q. Liang and J. Qiu, *RSC Adv.*, 2012, **2**, 2773-2779.
- 37 X. Xia, X. Dong, Q. Wei, Y. Cai and K. Lu, *Express Polym. Lett.*, 2011, **6**, 169-176.
- 38 P. Liu, J. Nisar, B. Pathak and R. Ahuja, *Int. J. Hydrogen Energy*, 2012, **37**, 11611-11617.
- 39 F. Dong, Y. Sun, M. Fu, W.-K. Ho, S. C. Lee and Z. Wu, *Langmuir*, 2011, **28**, 766-773.

- 40 H. Liu, W. Cao, Y. Su, Y. Wang and X. Wang, *Appl. Catal. B*, 2012, **111-112**, 271-279.
- 41 C. Yu, J. C. Yu, C. Fan, H. Wen and S. Hu, *Mater. Sci. Eng. B*, 2010, **166**, 213-219.
- 5 42 L. Jing, Y. Ou, B. Wang, S. Li, B. Jiang, L. Yang, W. Fu, H. Fu and J. Sun, *Sol. Energy Mater. Sol. Cells*, 2006, **90**, 1173-1787.
- 43 B. G. Yacobi and D. B. Holt, *Cathodoluminescence Microscopy of Inorganic Solids*, Plenum Press, New York, 1990.
- 10 44 H. Yu, S. Ouyang, S. Yan, Z. Li, T. Yu and Z. Zou, *J. Mater. Chem.*, 2011, **21**, 11347-11351.
- 45 Z. Ai, L. Zhang and S. Lee, *J. Phys. Chem. C*, 2010, **114**, 18594-18600.
- 15 46 Z. Ai, W. Ho and S. Lee, *J. Phys. Chem. C*, 2011, **115**, 25330-25337.
- 47 J. Huang, W. Cheuk, Y. Wu, F. S. C. Lee and W. Ho, *Catal. Sci. Technol.*, 2012, **2**, 1825.
- 48 B. Liu, K. Nakata, S. Liu, M. Sakai, T. Ochiai, T. Murakami, 20 K. Takagi and A. Fujishima, *J. Phys. Chem. C*, 2012, **116**, 7471-7479.